Processing and Application of Ceramics 16 [4] (2022) 374–383
https://doi.org/10.2298/PAC2204374I

Optimization of $La_{0.6}Sr_{0.4}Co_{0.2}Fe_{0.8}O_{3-\alpha}$ – $Ba(Ce_{0.6}Zr_{0.4})_{0.9}Y_{0.1}O_{3-\delta}$ cathode composition for proton ceramic fuel cell application

Ismariza Ismail[1,2], Nurul Izzati Abd Malek[3], Abdul Mutalib Md Jani[3,4], Mohd Hafiz Dzarfan Othman[5], Nafisah Osman[3,6,*]

[1]*Faculty of Chemical Engineering Technology, Universiti Malaysia Perlis, 02100 Padang Besar, Perlis, Malaysia*
[2]*Center of Excellence Geopolymer and Green Technology, School of Materials Engineering, Universiti Malaysia Perlis, 01000 Kangar, Perlis, Malaysia*
[3]*Proton Conducting Fuel Cell Research Group, Faculty of Applied Sciences, 40450 Shah Alam, Selangor, Malaysia*
[4]*Faculty of Applied Sciences, Universiti Teknologi MARA, 35400 Tapah Road, Tapah Perak, Malaysıa*
[5]*Advanced Membrane Technology Research Centre (AMTEC), School of Chemical & Energy Engineering, Faculty of Engineering, Universiti Teknologi Malaysia, 81310 UTM Skudai, Johor, Malaysia*
[6]*Faculty of Applied Sciences, Universiti Teknologi MARA, 02600 Arau, Perlis, Malaysia*

Received 9 May 2022; Received in revised form 26 August 2022; Accepted 27 October 2022

Abstract

Composite cathodes consisting of different compositional ratios of $La_{0.6}Sr_{0.4}Co_{0.2}Fe_{0.8}O_{3-\alpha}$ (LSCF) and $Ba(Ce_{0.6}Zr_{0.4})_{0.9}Y_{0.1}O_{3-\delta}$ (BCZY64), namely 100LSCF:0BCZY64 (L10B0), 70LSCF:30BCZY64 (L7B3), 50LSCF:50BCZY64 (L5B5) and 30LSCF:70BCZY64 (L3B7) were prepared via wet chemistry method. The symmetrical cell with a configuration of electrode|BCZY64|electrode was fabricated using dry-pressing method for the electrolyte substrate and spin-coating technique for the cathode layer. The proton conduction in the composite cathode increases as the amount of proton-conducting phase increases as verified by the water uptake measurement performed via thermogravimetric analysis. The thickness of the composite cathode layer is about 15 μm as observed by a scanning electron microscope and exhibits a well-connected particle network with sufficient porosity for oxidant diffusion (20–30%). The electrochemical performance of the symmetrical cell was investigated by electrochemical impedance spectroscopy in humidified air. The area-specific resistance (ASR) values of the tested cathodes follow the order of L7B3 < L10B0 < L5B5 < L3B7 and are 0.07 < 0.24 < 0.30 < 0.52 Ω·cm^2 at 700 °C, respectively. The correlation between the cathode performance and cathode composition was investigated and the corresponding mechanism was systematically postulated.

Keywords: *perovskite, fuel cell, electrodes, composite cathode, impedance spectroscopy*

I. Introduction

The proton ceramic fuel cell (PCFC) is an environmentally friendly technology that uses electrochemical processes to turn the chemical energy of the fuel into power. The qualities of the anode, cathode and electrolyte, which make up a PCFC's primary components, substantially impact the device's performance. Among the components, the cathode is a crucial part of the cell and has a consequential impact on the overall performance of a PCFC. Therefore, developing a good cathode material becomes critically significant in advocating PCFC performance. In the early stage of fuel cell development, platinum was employed as the cathode material. However, its high cost and non-negligible overpotential at high operating temperatures make it unsuitable for practical application [1–3]. The use of conductive metal oxides has then emerged as a viable alternative. As a result, mixed ionic and electronic conducting (MIEC) oxides have been extensively investigated as prospective cathodes for PCFC [4–6].

* Corresponding author: tel: +604 9882272
e-mail: *fisha@uitm.edu.my*

MIEC materials have attracted attention due to the high ambipolar conductivity that allows the extension of the cathode reaction sites beyond the triple-phase boundaries, hence offering greater performance as compared to the predominantly electronic conductor such as platinum. Several perovskite materials such as $Ba_{0.5}Sr_{0.5}Co_{0.8}Fe_{0.2}O_{3-\delta}$ (BSCF) [7,8], $Ba_{0.6}Sr_{0.4}Co_{0.9}Nb_{0.1}O_{3-\delta}$ (BSCN) [9], $Sm_{0.5}Sr_{0.5}CoO_{3-\delta}$ (SSC) [10] and $La_{0.6}Sr_{0.4}Co_{0.2}Fe_{0.8}O_{3-\delta}$ (LSCF) [11,12] have been thoroughly explored as potential PCFC cathodes. Among these, the lanthanum strontium cobalt ferrite oxide compounds, $La_{1-x}SrxCo_{1-y}Fe_yO_{3-\delta}$ (LSCF), have attracted large interest due to their high catalytic activity towards oxygen reduction, high oxygen self-diffusion coefficients and high ionic and electronic conductivity [12,13]. The encouraging performances suggest the potential of LSCF as a promising cathode material for PCFC.

MIEC materials exhibit satisfactory cathode performance in PCFC at an intermediate temperature range. However, the performance is inadequate for practical application due to the limited active reaction sites for the cathode reaction. Since the cathode reaction process in PCFC involves three types of charge carriers, which are proton (H^+), oxygen ion (O^{2-}), and electron (e^-), it is favourable that a cathode material for PCFC possesses simultaneous conduction of these three charge carrier species. These ideal cathode properties could be achieved by the incorporation of the proton-conducting phase into MIEC oxides to form a composite cathode [14–16].

The formulation of a composite cathode provides the extension of the triple-phase boundary (TPB), resulting in a great increase in the number of reaction sites that can facilitate the electrochemical reactions involving oxygen ions, protons and electrons. Consequently, enhanced cathode performance is envisaged. Tremendous research has been devoted to the development of the composite cathode. However, most studies have focused on material selection [15,16], fabrication [14,17] and microstructure [18,19] rather than on the reaction mechanism of the composite cathode. Furthermore, the elucidation of the role of the phase constituents in the composite cathode system is still lacking. The understanding of the processes that occurs at the composite cathode/electrolyte interface is important as the rates of many chemical and energy transformation processes are limited by the charge and mass transfer along surfaces and across interfaces.

Herein, the composite cathode comprising $La_{0.6}Sr_{0.4}Co_{0.2}Fe_{0.8}O_{3-\alpha}$ (LSCF) and $Ba(Ce_{0.6}Zr_{0.4})_{0.9}Y_{0.1}O_{3-\delta}$ (BCZY64) proton conductor was evaluated as a potential cathode material for PCFC based on BCZY64 electrolyte. The impact of the various compositional ratios between MIEC and the proton conductive phase in terms of proton concentration and water formation that affect the cathode performance was discussed. Additionally, the correlations between the composite cathode composition and the cathode reaction mechanism were systematically postulated.

II. Experimental

2.1. Powder synthesis

For synthesis of $La_{0.6}Sr_{0.4}Co_{0.2}Fe_{0.8}O_{3-\alpha}$ (LSCF) cathode, a stoichiometric amounts of $La(NO_3)_3 \cdot 6H_2O$ (99.9%, ACROS), $Sr(NO_3)_2$ (99%, ACROS), $Co(NO_3)_2 \cdot 6H_2O$ (99%, ACROS) and $Fe(NO_3)_3 \cdot 9H_2O$ (99%, ACROS) were dissolved in 100 ml of deionized water. Citric acid monohydrate (CA) (99.5%, MERCK) and ethylene diamine tetra-acetic acid (EDTA) (99%, ACROS) were subsequently added, and the solution was heated at 70 °C in water bath under continuous stirring. Ethylene glycol was then added to the mixture solution according to the molar ratio of 0.7 : 1 (ethylene glycol : LSCF). The obtained gel was calcined at 700 °C for 5 h to prepare a pure LSCF phase. The enhanced electrochemical performance of modified LSCF over unmodified LSCF has been thoroughly discussed and reported in our previous work [20]. For the electrolyte, the $Ba(Ce_{0.6}Zr_{0.4})_{0.9}Y_{0.1}O_{3-\delta}$ (BCZY64) powder was synthesized by a combined citrate-EDTA sol-gel method [21]. Fabrication of the composite cathode was performed by mixing single phases of both powders in different LSCF:BCZY64 weight ratios, namely 100:0, 70:30, 50:50 and 30:70 which are respectively denoted as L10B0, L7B3, L5B5 and L7B3 (Table 1). The mixtures were ground in an agate mortar with acetone to facilitate the mixing process and subsequently dried in an oven at 100 °C for 3 h.

Table 1. Notation of the composite cathode samples

Cathode ID	Composition [wt.%] LSCF	BCZY64
L10B0	100	0
L7B3	70	30
L5B5	50	50
L3B7	30	70

2.2. Powder characterization

The water uptake analysis of the calcined powders was performed by using a thermal gravimetric analyser (TGA, Perkin Elmer STA 600) with a purified air flow (100 ml/min) ($p_{H_2O} \approx 0.03$ atm) at a heating rate of 5 °C/min. Before the analysis, the sample was hydrated in the ambient air (40–45% humidity) at 27 °C for 7 days. The weight loss was evaluated as a function of temperature, which ranged from 30 to 800 °C. The microstructure and elemental analysis of the fabricated symmetrical cell were studied by a scanning electron microscope (SEM) imaging and energy dispersive X-ray (EDX) analysis (JEOL JSM 6460LA). The porosity of the sintered cathode layers was estimated by an image analysis software (ImageJ 1.45p) using the thresh-

old technique. The compositional ratio of the composite cathode constituents was calculated from X-ray diffraction peaks intensity using EVA XRD analysis software (Bruker-AXS, Germany).

2.3. Fabrication of symmetrical cell

A dense BCZY64 electrolyte pellet for a symmetrical cell fabrication was obtained by uniaxial compression at 5 tons, followed by a two-step sintering (TSS) at T_1 = 1500 °C (1 min) and T_2 = 1450 °C (12 h) in the air [22]. The pellet was then polished with silicon carbide (SiC) polishing paper grit #400 and the slurry of the cathode material was coated by spin-coating on both sides of the pellet. Finally, the obtained symmetrical cell was annealed at 950 °C for 3 h with heating and cooling rates of about 10 °C/min.

2.4. Performance test

The electrochemical characteristics of the symmetrical cell (Cathode ID|BCZY64|Cathode ID) were tested by electrochemical impedance spectroscopy (EIS) using ZIVE SP2 Electrochemical Workstation (ZIVE LAB SP2, WonATech). EIS spectra were collected in the 0.01 Hz to 1 MHz frequency range with a signal amplitude of 10 mV under open-circuit conditions. The EIS measurement was conducted in humidified air ($p_{H_2O} \approx$ 0.03 atm) over a temperature range of 500 to 800 °C. Before the measurement, the cell was exposed to the humidified air at 700 °C for 24 h and stabilized for 1 h to achieve the equilibrium condition for each measurement temperature.

EIS spectra analysis was carried out using the ZMAN software. The fitting and simulation procedure using ZMAN software was implemented to precisely identify the electrolyte and cathode responses from the spectrum. The area-specific resistance (ASR) of the electrode reactions was calculated using the relation $ASR = R_p \cdot S/2$, where S is defined as the effective surface area of the electrode and the factor 1/2 takes into account that symmetrical cells used. The associated capacitance (C) and the arc summit frequencies (f^0) of each contribution, which are two critical parameters to identify the processes involved in the cathode reactions, were calculated using Eqs. 1 and 2:

$$C = Y^{\frac{1}{n}} \cdot R^{\frac{1}{n}-1} \quad (1)$$

$$f^0 = \frac{1}{2}\pi \cdot R \cdot C \quad (2)$$

where Y and n refer to the parameters associated with the constant phase element which are obtained from the fitting process.

III. Results and discussion

TGA water uptake analysis was performed to access the hydration capacity and predict the proton conduction in the composite cathodes. The hydration capacity signifies the ability of the sample to locate protons thus indicating the proton concentration in the composite cathode sample. A high proton concentration would assist in proton conduction and thus extend the triple-phase boundary which is the active site for the electrochemical reaction [23]. Therefore, the water uptake analysis is important to verify the proton concentration in the cathode sample upon the addition of different BCZY64 amounts. TGA dehydration curves of the four cathode samples are shown in Fig. 1. Weight loss of the L10B0 sample is only 0.2%. However, with the addition of 30 vol.% (L7B3) and 50 vol.% (L5B5) of the BCZY64 phase into the cathode, the amount of weight loss increased to 3.6% and 3.8%, respectively. A significant weight loss of 5.1% was obtained for the L3B7 sample, thus corroborating the highest proton concentration in this sample compared to other composite cathodes. The large proton concentration in this sample suggests high proton conduction in the cathode material which leads to the extension of the triple-phase boundary and potentially accelerates the cathode reactions [12]. This suggestion is supported by the EIS measurement and the proposed cathode reaction mechanism is discussed later.

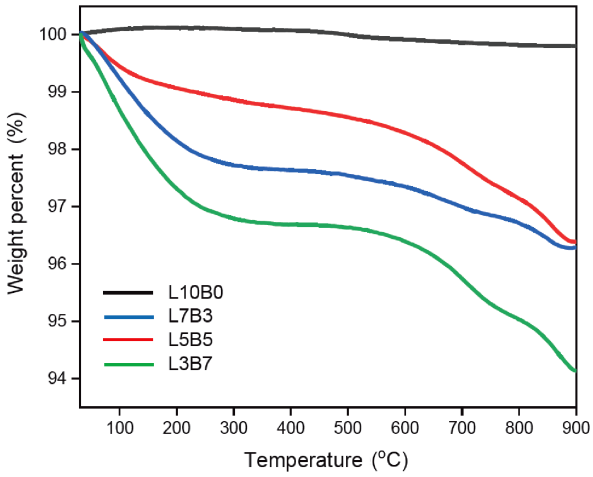

Figure 1. TGA curves of hydrated cathode samples in flowing air

Figure 2 shows cross-sectional SEM images of the composite cathodes on the BCZY64 electrolyte. As it can be seen, all composite cathodes have a good adherence to the BCZY64 electrolyte with no signs of cracking and delamination, suggesting a good thermal matching between parts. The thicknesses of the electrolyte and composite cathode layers in all symmetrical cells is about 1 mm and 15 μm, respectively. The microstructures of the composite cathode in all cells are comparatively similar, exhibiting a well-connected particle network and sufficient porosity for oxidant diffusion (20–30%). Therefore, with the relatively similar electrolyte thickness and very close cathode microstructure, the different cell performances should be attributed to the intrinsic properties of the varying composition of the composite cathode.

EDX analysis was used to estimate the elemental composition and the compositional ratio of the com-

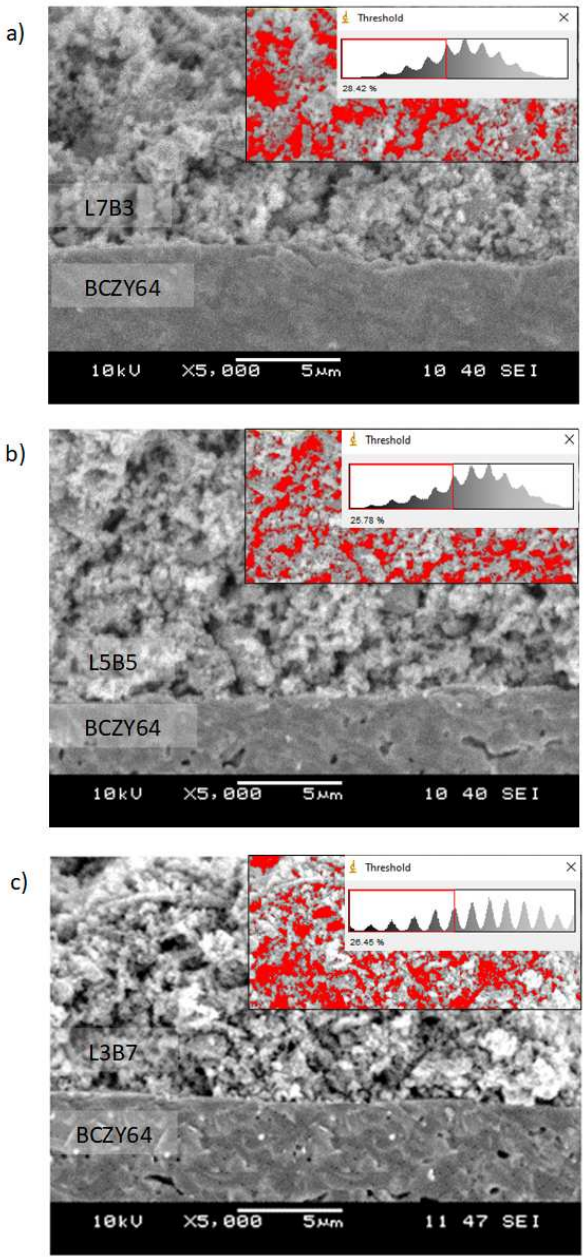

Figure 2. SEM cross-sectional image of the fractured symmetrical cells: a) L7B3, b) L5B5 and c) L3B7 composite cathodes after firing at 950 °C

posite cathode materials. Elemental compositions of the cathode and electrolyte layer of the symmetrical cells are summarized in Table 2. Compositions of the cathode and electrolyte layers are very close to the stoichiometric ratio of LSCF and BCZY64 materials (La = 0.6, Sr = 0.4, Co = 0.2 and Fe = 0.8 for LSCF and Ba = 1.00, Ce = 0.54, Zr = 0.36 and Y = 0.10 for BCZY64). The composite cathodes consist of a gradually increasing BCZY64 and decreasing LSCF contents as the proton-conducting phase concentration increases from L7B3 to L3B7. The value of the phase compositional ratio obtained from EDX analysis follows the estimated value from the XRD peak intensity analysis reported in our previous work [24]. The comparison between the nominal and the estimated compositional ratio from the XRD peak analysis is shown in Table 3. As it can be seen, there is a slight deviation in the nominal and estimated values of the composition, which is expected due to the limitation of the quantitative analysis using XRD. The composition was estimated based on the intensity of the diffraction peaks, since it is known to be proportional to the concentration of the material. However, the peak intensity might be influenced by other factors that may cause overestimation or underestimation of a particular phase in the sample [25]. Despite the slight deviation, there is substantial agreement between the nominal and estimated values, thus indicating that the composition of the composite cathode constituents is preserved even after high-temperature treatment.

Figure 3 illustrates the typical Nyquist plots of the symmetrical cell with an LSCF single cathode and LSCF-BCZY64 composite cathodes over the temperature range of 500–800 °C. The presence of overlapping semicircles indicates more than one electrochemical process. EIS spectra obtained for the composite cathodes were resolved into three different regions, which are high frequency (HF; 1 MHz–1 kHz), middle frequency (MF; 1 kHz–1 Hz), and low frequency (LF; 1 Hz–10 mHz) regions. The size of the EIS spectrum decreases as the temperature increases (Fig. 3). This observation shows the dependency of the involved reactions on the operating temperature and signifies that the corresponding electrochemical reactions are thermally activated processes. Furthermore, it is also noticeable that the sizes of the EIS spectra for the composite cathodes are smaller than for the pristine sample (L10B0), which suggests a different electrochemical characteristics of the cathode samples. These initial EIS findings indicate that the difference in the cathode composition significantly affects the electrochemical characteristics of the tested cathodes.

For the L10B0 cathode (Fig. 3a), the impedance arcs at the lower frequencies seem to dominate the whole spectrum, thus suggesting that the cathode activity is limited by the oxygen species reactions at the cathode [26]. A similar observation was obtained for the L7B3 sample (Fig. 3b), which infers the high contribution of the low-frequency cathode reaction on the overall cathode performance. On the contrary, for the L5B5 and L3B7 cathodes (Figs. 3c,d), the higher frequency arc seems to dominate the spectrum, suggesting that ionic conduction probably limits the cathode reaction [27,28]. Moreover, it is also observable from the spectra that the size of the impedance arcs becomes larger as the BCZY64 content in the composite cathode increases from 30 to 70 wt.%, as shown in Figs. 3b-d. This observation suggests a higher impedance value, implying a higher cathode resistivity with increasing BCZY64 content in the L5B5 and L3B7 composite cathodes.

The EIS fitting results for the composite L7B3, L5B5 and L3B7 cathodes at 500 °C are presented in Fig. 4. Each spectrum was fitted to a matching equivalent cir-

Table 2. Elemental composition of the composite cathode symmetrical cells

Cells Component	Element	Elemental atomic percentage [%]		
		L7B3	L5B5	L3B7
Cathode layer	La	10.61 ± 0.06	4.46 ± 0.05	1.42 ± 0.02
	Sr	5.03 ± 0.08	2.98 ± 0.17	1.63 ± 0.02
	Co	1.96 ± 0.11	0.51 ± 0.07	0.42 ± 0.08
	Fe	8.23 ± 0.10	3.40 ± 0.09	1.17 ± 0.04
	Ba	13.22 ± 0.10	15.72 ± 0.25	17.20 ± 0.35
	Ce	7.61 ± 0.06	8.87 ± 0.13	10.31 ± 0.15
	Zr	4.88 ± 0.15	5.80 ± 0.22	5.98 ± 0.11
	Y	1.23 ± 0.15	1.90 ± 0.10	2.29 ± 0.29
	O	47.21 ± 1.01	56.37 ± 0.63	59.58 ± 0.57
Electrolyte layer	Ba	24.98 ± 0.66	23.81 ± 0.55	24.47 ± 0.34
	Ce	12.67 ± 0.30	12.29 ± 0.41	12.20 ± 0.24
	Zr	7.50 ± 0.40	7.53 ± 0.30	7.51 ± 0.32
	Y	42.70 ± 0.25	2.75 ± 0.22	3.03 ± 0.18
	O	52.15 ± 1.00	53.64 ± 0.51	52.80 ± 0.46

Table 3. Comparison between the nominal and the estimated compositional ratio of the composite cathodes

Cathode ID	Nominal composition (LSCF:BCZY64)	Estimated composition (LSCF:BCZY64)
L7B3	70:30	70:30
L5B5	50:50	42:58
L3B7	30:70	22:78

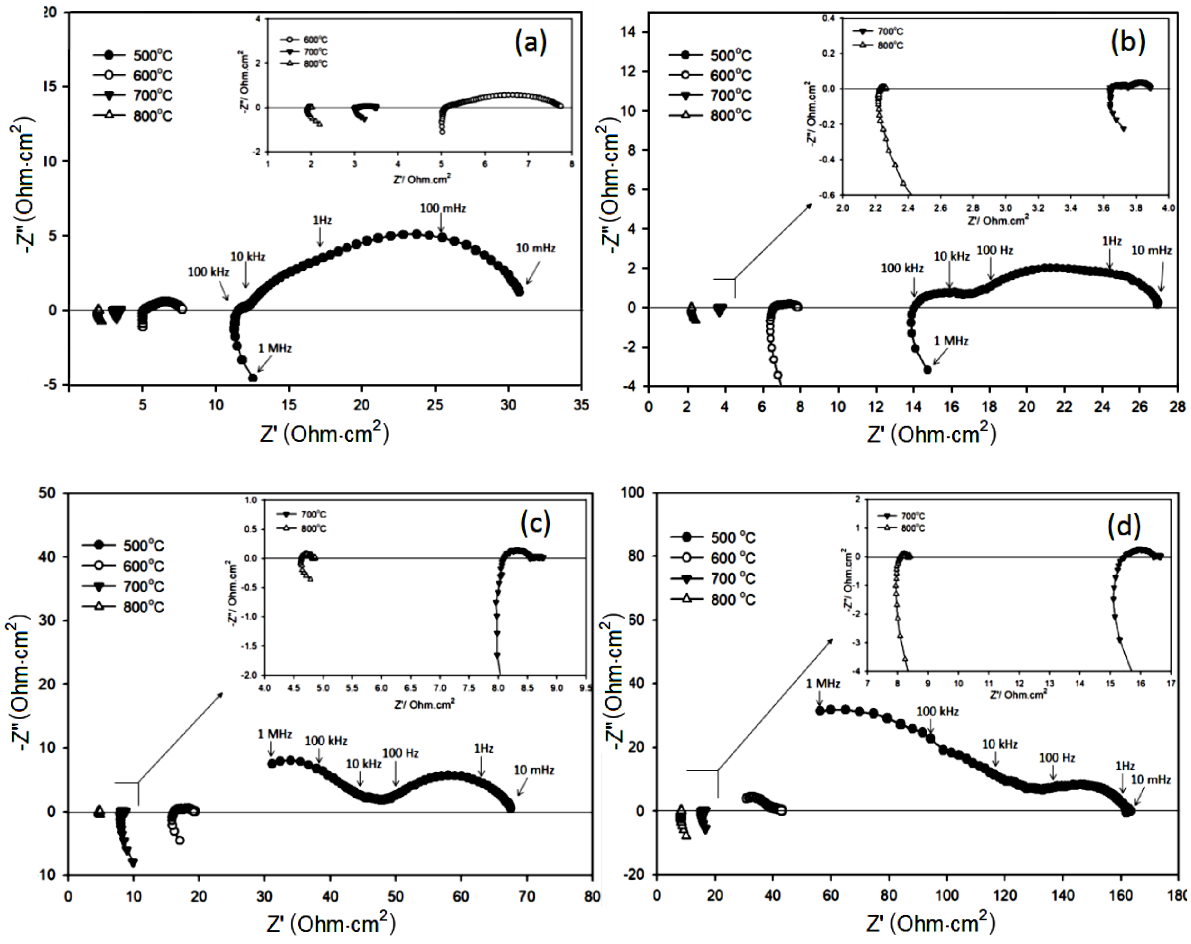

Figure 3. Typical Nyquist plot for: a) L10B0, b) L7B3, c) L5B5 and d) L3B7 composite cathodes measured at 500–800 °C in humidified air

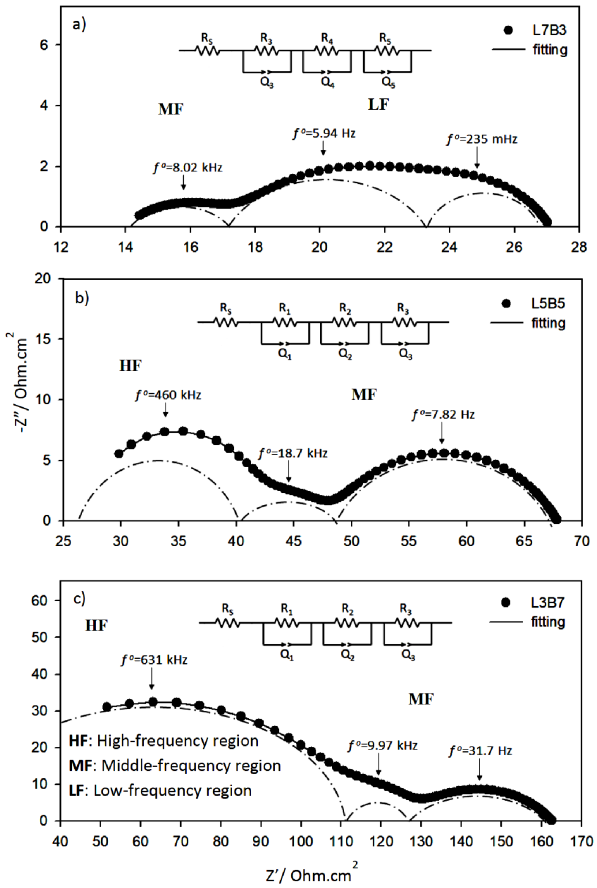

Figure 4. Fitting of EIS spectra for: a) L7B3, b) L5B5 and c) L3B7 composite cathodes measured at 500 °C in humidified air

cuit as shown in the inset in Fig. 4, where R_s is the total ohmic resistance, R_1Q_1 refers to the grain boundary response, R_2Q_2 and R_3Q_3 correspond to the middle frequency cathode responses, and R_4Q_4 and R_5Q_5 are associated with the low-frequency cathode processes. R and Q respectively denote resistance and constant phase element (CPE) in the circuit. The values of the circuit elements calculated from the fitting results of the composite cathodes are presented in Table 4.

The obtained impedance arcs were allocated to their corresponding processes using the capacitance (C) values related to each arc. Figure 4a presents the EIS spectrum for the L7B3 composite cathode consisting of three arcs ascending at the middle and low-frequency regions of the spectrum. The first arc (R_3Q_3, $C \approx 10^{-6}$ F·cm^2) observed at the middle frequency region is associated with the cathode charge transfer reaction, whereas the arcs at the low-frequency region (R_4Q_4 and R_5Q_5, $C \approx 10^{-2}$–10^{-3} F·cm^2) are attributed to the oxygen adsorption/dissociation and diffusion processes at the cathode. The capacitance values obtained from the analyses agree with the literature data concerning related works [29–31].

For the composite cathode containing 50 wt.% of BCZY64 (L5B5), the spectrum was resolved to three consecutive arcs, as shown in Fig. 4b. The first high-frequency arc (R_1Q_1, $C \approx 10^{-8}$ F·cm^2) corresponds to the grain boundary contribution, whereas the arcs in the middle frequency range (R_2Q_2 and R_3Q_3, $C \approx 10^{-4}$–10^{-7} F·cm^2) were attributed to the cathode charge transfer reactions. The dominant responses observed at the middle frequency region suggest that the electrochemical activities of the L5B5 at 500 °C are probably limited by the charge transfer reactions at the cathode/electrolyte interface, which agrees with other related works in the literature [28,32].

The EIS spectrum of the L3B7 composite cathode also consists of three consecutive arcs (Fig. 4c). It exhibits a significant contribution of the electrolyte grain boundary at the high-frequency region, which was denoted as R_1Q_1 ($C \approx 10^{-9}$ F·cm^2) in the equivalent circuit. Like the L5B5 cathode, only grain boundary response and charge transfer responses (R_2Q_2 and R_3Q_3, $C \approx 10^{-5}$–10^{-7} F·cm^2) were evident from the EIS spectrum of this cathode sample. As it can be seen from the spectra in Figs. 4b,c, the middle-frequency impedance arcs, which correspond to the charge transfer processes, become more prominent as the content of BCZY64 increases. The size increment of the impedance arcs suggests an increase in the resistivity of the charge transfer reaction with the increased amount of the pro-

Table 4. Values of the circuit elements calculated from the fitting results of the composite cathodes at 500 °C

Composite cathode	Resistance R_p [Ω·cm^2]	Capacitance C [F·cm^2]	Arc summit requencies f^0 [Hz]
L10B0	R_3 : 4.97 ± 0.09	C_3 : (5.67 ± 0.04) × 10^{-3}	f_3^0 : 2.82 ± 0.07
	R_4 : 14.30 ± 0.09	C_4 : (4.78 ± 0.01) × 10^{-2}	f_4^0 : 0.12 ± 0.01
L7B3	R_3 : 3.67 ± 0.08	C_3 : (1.35 ± 0.06) × 10^{-6}	f_3^0 : (8.02 ± 0.11) × 10^3
	R_4 : 5.87 ± 0.14	C_4 : (1.14 ± 0.18) × 10^{-3}	f_4^0 : 5.94 ± 0.42
	R_5 : 3.62 ± 0.12	C_5 : (4.67 ± 0.35) × 10^{-2}	f_5^0 : 0.24 ± 0.04
L5B5	R_1 : 12.96 ± 0.49	C_1 : (1.08 ± 0.21) × 10^{-8}	f_1^0 : (4.60 ± 0.01) × 10^5
	R_2 : 8.43 ± 0.49	C_2 : (4.09 ± 0.07) × 10^{-7}	f_2^0 : 1.87 ± 0.01) × 10^4
	R_3 : 19.44 ± 0.50	C_3 : (4.29 ± 0.23) × 10^{-4}	f_3^0 : 7.82 ± 0.18
L3B7	R_1 : 99.20 ± 0.71	C_1 : (1.04 ± 0.08) × 10^{-9}	f_1^0 : (6.31 ± 0.01) × 10^4
	R_2 : 15.04 ± 0.18	C_2 : (4.35 ± 0.12) × 10^{-7}	f_2^0 : (9.97 ± 0.02) × 10^3
	R_3 : 35.21 ± 0.32	C_3 : (5.84 ± 0.08) × 10^{-5}	f_3^0 : (3.17 ± 0.01) × 10^1

Table 5. Area specific resistance (*ASR*) for the single and composite cathode samples measured at 500–800 °C

Operating temperature [°C]	*ASR* [Ω·cm^2]			
	L10B0	L7B3	L5B5	L3B7
500	9.64 ± 0.03	6.57 ± 0.06	13.93 ± 0.24	25.12 ± 0.21
600	1.31 ± 0.03	0.47 ± 0.01	1.43 ± 0.06	2.47 ± 0.09
700	0.24 ± 0.02	0.07 ± 0.02	0.30 ± 0.03	0.52 ± 0.05
800	0.04 ± 0.01	0.02 ± 0.01	0.10 ± 0.03	0.20 ± 0.03

ton conductor in the composite cathode. These large impedance arcs might have significantly suppressed the low-frequency response, which indicates that the slow interfacial charge transfer reactions primarily limit the electrochemical performance of the cathode at the measured temperature. Similar observations were also reported in the previous related work [33].

The electrode resistance (R_p) was obtained as the sum of the resistances calculated from the semicircles in the middle and low-frequency ranges. The cathode performance of the composite cathodes in terms of *ASR* measured at 500–800 °C is summarized in Table 5, together with the *ASR* of the L10B0 cathode to facilitate the comparison. The L7B3 cathode exhibits much lower *ASR* values than the L10B0 and other tested composite cathodes. In contrast, the composite cathode with the highest content of BCZY64 protonic conductor, the L3B7 cathode, shows the highest *ASR* values at all measured temperatures. It can be observed that the incorporation of 30 wt.% of BCZY64 protonic conductor in the L7B3 composite cathode has substantially reduced *ASR* value of the LSCF cathode. However, a further increase in the BCZY64 content to 50 and 70 wt.% results in poor performance of the composite cathode, which could be evidenced by a marked increase of*ASR* values for the L5B5 and L3B7 compared to the L7B3 cathode. Based on *ASR* values, the L7B3 cathode demonstrated five- and ten-times higher performance than the L5B5 and L3B7, respectively, in the temperature range 500–800 °C. Besides, *ASR* value of the L7B3 was three and two folds lower than for the L10B0 at the measurement temperatures of 700 and 800 °C, respectively, which signifies the improved performance of the composite cathode. The reasons for these findings can be related to the conduction and percolation of the protonic, ionic and electronic phases in the composite cathode. For clarity, the proposed mechanism of the cathode reaction is illustrated in Fig. 5.

The cathode reaction mechanism of the L10B0 is shown in Fig. 5a. The L10B0 cathode is a mixed oxide ionic/electronic conducting (MIEC) material, allowing the conduction of electron and oxygen ionic species. Therefore, in the triple-phase boundary (TPB), the active reaction site is restricted to the interface between cathode/electrolyte only. Hence, the charged species involved in the cathode reaction, i.e. oxide ions, electrons and protons, have to find their pathways to the TPB region to complete the cathode reaction. A long transfer pathway generally results in higher polarization resistance, thus resulting in higher cathode *ASR* [34].

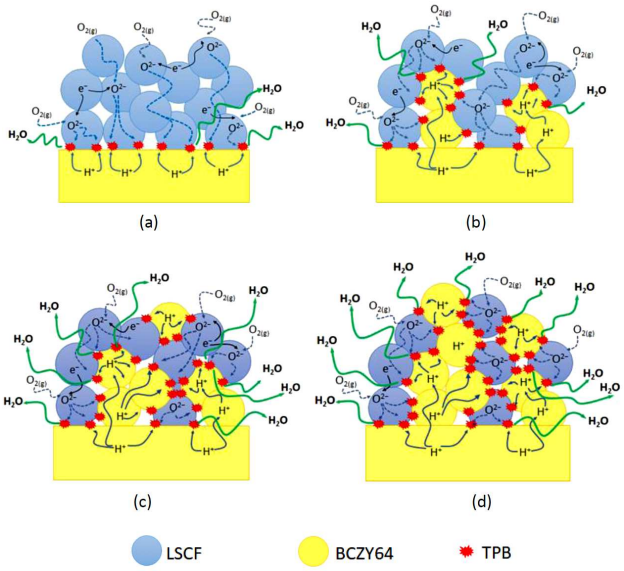

Figure 5. Schematic representation of the cathode reaction mechanism proposed for: a) L10B0, b) L7B3, c) L5B5 and d) L3B7 cathodes

The incorporation of 30 wt.% of BCZY64 protonic conductor in the LSCF to form the composite cathode, as in the sample L7B3 (Fig. 5b), was demonstrated to reduce *ASR* substantially. The performance enhancement of the L7B3 compared to LSCF can be ascribed mainly due to the introduction of proton-conducting percolation pathways, since it has been generally observed that the percolation threshold of a ceramic composite cathode for solid oxide fuel cell operation was around 30 wt.% [35,36]. Here, "percolation" is defined as the continuous connection of the protonic conducting path through the whole cathode structure. The introduction of a protonic conductive network, together with ionic and electronic pathways, promotes the extension of TPB areas allowing the electrochemical reaction to occur in a larger region of the cathode [37,38]. Therefore, as the TPB and transfer paths increase, the corresponding conducting species will choose the most convenient route to be transported and converted among each other to achieve minimal polarization resistance losses, which subsequently results in the accelerated oxygen reduction process.

In contrast, as content of the BCZY64 protonic conductor in the composite cathode increased to 50 and 70 wt.%, as shown in Figs. 5c,d respectively, the cathode performance was found to reduce significantly. The poor cathode performance exhibited by the L5B5 and L7B3 can be explained in terms of reduced connec-

Table 6. Comparison of the composite cathodes – performance based on proton-conducting electrolyte

Cathode material	Electrolyte material	p_{O_2}/n	T [°C]	ASR [Ω·cm^2]	Ref.
$La_{0.6}Sr_{0.4}Co_{0.2}Fe_{0.8}O_{3-\alpha}$ + $Ba(Ce_{0.6}Zr_{0.4})_{0.9}Y_{0.1}O_{3-\delta}$	$Ba(Ce_{0.6}Zr_{0.4})_{0.9}Y_{0.1}O_{3-\delta}$	0.5	700	0.07	This work
$Ba_{0.5}Sr_{0.5}Co_{0.8}Fe_{0.2}O_{3-\delta}$ + $BaZr_{0.1}Ce_{0.7}Y_{0.2}O_{3-\delta}$	$BaZr_{0.1}Ce_{0.7}Y_{0.2}O_{3-\delta}$	-	700	0.10	[47]
$Sm_{0.5}Sr_{0.5}FeO_{3-\delta}$ + $BaZr_{0.1}Ce_{0.7}Y_{0.2}O_{3-\delta}$	$BaZr_{0.1}Ce_{0.7}Y_{0.2}O_{3-\delta}$	-	700	0.10	[48]
$La_{0.6}Sr_{0.4}Co_{0.2}Fe_{0.8}O_3$ + $BaCe_{0.9}Y_{0.1}O_{3-\delta}$	$BaCe_{0.8}Y_{0.2}O_{3-\delta}$	0.5	700	0.14	[49]
$Nd_{1.95}NiO_{4+\delta}$ + $BaZr_{0.1}Ce_{0.7}Y_{0.1}Yb_{0.1}O_{3-\delta}$	$BaZr_{0.1}Ce_{0.7}Y_{0.1}Yb_{0.1}O_{3-\delta}$	0.4	750	0.43	[30]

tivity of the LSCF cathode particles in the composite cathode due to an excessive protonic conducting phase. Thus, the continuity of electronic and ionic conductions is interrupted, which eventually results in a lower cathode performance. Another possible reason that could be considered is the excess formation of water which results from the extension of the TPB areas. It is well known that the addition of a proton-conducting phase in an MIEC cathode would increase the TPB region, thus assisting the acceleration of the cathode electrochemical reactions. However, as the TPB increases, the water formation which results from the cathode reaction also increases. The high concentration of water vapour will severely dilute the oxidant (air or oxygen) and ultimately weaken the cathode electrocatalytic ability. In addition, excessive water generated in the cathode has been reported to be detrimental to the cathode performance as it can also increase polarization resistance and degrade cell performance [39–41]. This result indicates the inferior performance of the L5B5 and L7B3 cathodes compared to the L7B3 and L10B0 (pristine LSCF) cathodes.

Figure 6 presents the Arrhenius plots for *ASR* of the L10B0 and the composite L7B3, L5B5 and L3B7 cathodes measured at different temperatures. The activation energies (E_a), calculated from the slopes of the Arrhenius plots, were 1.30, 1.38, 1.18 and 1.16 eV for the L10B0, L7B3, L5B5 and L3B7 cathodes, respectively. The E_a value of the L7B3 was relatively close to LSCF mainly due to the presence of similar dominant conducting species in the cathode samples (L7B3 consists of

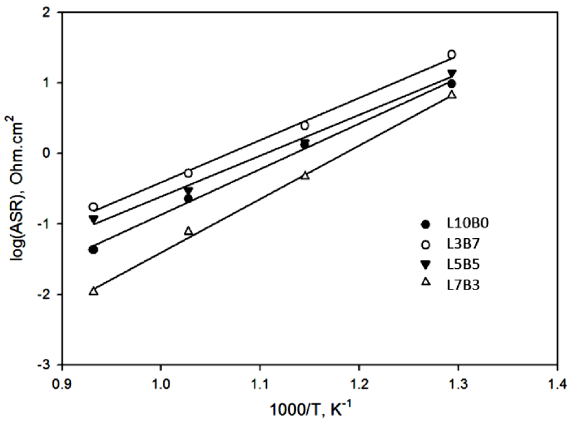

Figure 6. The Arrhenius plots for the *ASR* of the L10B0 and the composite cathodes measured at 500–800 °C

70 wt.% of LSCF). These E_a values are in reasonable agreement with prior studies of LSCF-based cathodes, as reported in the literature [42–44].

For L5B5 and L3B7, the activation energy values were lower than for the L10B0 and L7B3. The compositions of the samples are dominated by the proton-conducting phase of BCZY64, which has a relatively lower activation energy of proton conduction (~0.6 eV) as compared to the oxide ion conduction (~1.4 eV) in the L10B0. Therefore, the E_a of the L5B5 and L3B7 cathodes decrease as the amount of the protonic conductor in the composites increases. Even though the lowest activation energy was obtained for the L3B7, applying the cathode with such a composition is not practical due to its poor electrochemical performance. A similar trend of activation energies was already obtained for the composite cathodes based on proton-conducting electrolytes [45,46]. In summary, the electrochemical performances of the tested cathodes follow the order of L7B3 > L10B0 > L5B5 > L3B7.

The electrochemical performance of the L7B3 on the BCZY64 electrolyte is compared with other composite cathode materials based on proton-conducting electrolytes, especially the works focusing on the widely used electrolyte material of $BaZr_{0.1}Ce_{0.7}Y_{0.2}O_{3-\delta}$ (BCZY17) as a proton conductor. As shown in Table 6, *ASR* value of the composite cathode obtained in this study is lower and comparable with other related works reported on the PCFC cathode development. Lower *ASR* is indeed desirable for achieving high cathode performance. In addition, the application of the BCZY protonic conductor with novel composition of $Ba(Ce_{0.6}Zr_{0.4})_{0.9}Y_{0.1}O_{3-\delta}$ (BCZY64) in this study has revealed a great potential of these cathode/electrolyte materials combination as a superior composite cathode system for producing high performance PCFC.

IV. Conclusions

The addition of the BCZY64 protonic conductor in the LSCF to become an LSCF-BCZY64 composite cathode is favourable in enhancing the cathode performance. However, the amount of the protonic conductor must be carefully controlled as sufficient MIEC cathode loading is essential to provide the electronic conducting paths and oxide ionic conduction to lengthen electrochemical reaction sites for the oxygen reduction process. Furthermore, the increases of the reaction sites

caused by the excessive addition of the protonic conductor will indirectly lead to excess water formation in the composite cathode, thus increasing the polarization resistance and eventually causing it to perform even worse than the pristine LSCF cathode. The best cathode performance was obtained for the L7B3, with an *ASR* of $0.07\,\Omega{\cdot}cm^2$ at 700 °C. These findings indicate that the coexisting sites of the electronic, oxygen ionic and protonic conducting phases in optimum ratios are crucial for the electrochemical reactions at the cathodes.

Acknowledgements: This research was supported by a Strategic Research Partnership (SRP) Grant UiTM-UTM (100-RMC 5/3/SRP GOV (002/2021)) and Fundamental Research Grant Scheme (FRGS) (FRGS/1/2020/STG04/UNIMAP/02/2). The authors thank Universiti Teknologi MARA and Universiti Malaysia Perlis for the facilities and support provided.

References

1. H. Uchida, S. Tanaka, H. Iwahara, "Polarization at Pt electrodes of a fuel cell with a high temperature-type proton conductive solid electrolyte", *J. Appl. Electrochem.*, **15** [1] (1985) 93–97.
2. E. Fabbri, A. D'Epifanio, E. Di Bartolomeo, S. Licoccia E.Traversa, "Tailoring the chemical stability of $Ba(Ce_{0.8-x}Zr_x)Y_{0.2}O_{3-\delta}$ protonic conductors for intermediate temperature solid oxide fuel cells (IT-SOFCs)", *Solid State Ionics*, **179** [15] (2008) 558–564.
3. R.M. Ormerod, "Solid oxide fuel cells", *Chem. Soc. Rev.*, **32** [1] (2003) 17–28.
4. A. Esquirol, N.P. Brandon, J.A. Kilner, M. Mogensen, "Electrochemical characterization of $La_{0.6}Sr_{0.4}Co_{0.2}Fe_{0.8}O_3$ cathodes for intermediate-temperature SOFCs", *J. Electrochem. Soc.*, **151** [11] (2004) A1847–A1855.
5. D.Z. de Florio, R. Muccillo, V. Esposito, E. Di Bartolomeo, E. Traversa, "Preparation and electrochemical characterization of perovskite/YSZ ceramic films", *J. Electrochem. Soc.*, **152** [1] (2004) A88.
6. E. Boehm, A. McEvoy, "Protonic electroceramics for fuel cells", *Fuel Cells*, **6** [1] (2006) 54–58.
7. X. Yhang, W. Wang, D. Zhang, Y. Jiang, X. Zhou, B. Lin, "A Zn-doped $Ba_{0.5}Sr_{0.5}Co_{0.8}Fe_{0.2}O_{3-\delta}$ perovskite cathode with enhanced ORR catalytic activity for SOFCs", *Catalysts*, **10** [2] (2020) 235.
8. W. Liu, H. Kou, X. Wang, L. Bi, X.S. Zhao, "Improving the performance of the $Ba_{0.5}Sr_{0.5}Co_{0.8}Fe_{0.2}O_{3-\delta}$ cathode for proton-conducting SOFCs by microwave sintering", *Ceram. Int.*, **45** [16] (2019) 20994–20998.
9. Y. Lin, R. Ran, D. Chen, Z. Shao, "A novel $Ba_{0.6}Sr_{0.4}Co_{0.9}Nb_{0.1}O_{3-\delta}$ cathode for protonic solid-oxide fuel cells", *J. Power Sources*, **195** [15] (2010) 4700–4703.
10. T. Wu, Y. Zhao, R. Peng, C. Xia, "Nano-sized $Sm_{0.5}Sr_{0.5}CoO_{3-\delta}$ as the cathode for solid oxide fuel cells with proton-conducting electrolytes of $BaCe_{0.8}Sm_{0.2}O_{2.9}$", *Electrochim. Acta*, **54** [21] (2009) 4888–4892.
11. S. Sun, Z. Cheng, "Electrochemical behaviors for Ag, LSCF and BSCF as oxygen electrodes for proton conducting IT-SOFC", *J. Electrochem. Soc.*, **164** [10] (2017) F3104.
12. Y.-W. Lai, K.-R. Lee, S.-Y-Yang, C.-J. Tseng, S.-C. Jang, I.-Y. Tsao, S.-Y. Chen, S.-W. Lee, "Production of $La_{0.6}Sr_{0.4}Co_{0.2}Fe_{0.8}O_{3-\delta}$ cathode with graded porosity for improving proton-conducting solid oxide fuel cells", *Ceram. Int.*, **45** [17] (2019) 22479–22485.
13. S. Upasen, P. Batocchi, F. Mauvy, A. Slodczyk, P. Colomban, "Chemical and structural stability of $La_{0.6}Sr_{0.4}Co_{0.2}Fe_{0.8}O_{3-\delta}$ ceramic vs. medium/high water vapor pressure", *Ceram. Int.*, **41** [10] (2015) 14137–14147.
14. H. Dai, E.H. Da'as, S.P. Shafi, H. Wang, L. Bi, "Tailoring cathode composite boosts the performance of proton-conducting SOFCs fabricated by a one-step co-firing method", *J. Eur. Ceram. Soc.*, **38** [7] (2018) 2903–2908.
15. Y. Bu, S. Joo, Y. Zhang, Y. Wang, D. Meng, X. Ge, G. Kim, "A highly efficient composite cathode for proton-conducting solid oxide fuel cells", *J. Power Sources*, **451** (2020) 227812.
16. B. Liu, L. Jia, B. Chi, J. Pu, J. Li, "A novel $PrBaCo_2O_{5+\sigma}$-$BaZr_{0.1}Ce_{0.7}Y_{0.1}Yb_{0.1}O_3$ composite cathode for proton-conducting solid oxide fuel cells", *Composites Part B Eng.*, **191** (2020) 107936.
17. M. Fu, K. Li, Y. Yang, Q. Zeng, L. Zeng, Z. Tao, "Fabrication and study of $LaNi_{0.6}Fe_{0.4}O_{3-\delta}$ and $Sm_{0.5}Sr_{0.5}CoO_{3-\delta}$ composite cathode for proton-conducting solid oxide fuel cells", *Sep. Purif. Technol.*, **287** (2022) 120581.
18. X. Xi, X. Chen, G. Hou, N. Xu, Q. Zhang, Z. Tao, "Fabrication and evaluation of $Sm_{0.5}Sr_{0.5}CoO_{3-\delta}$ impregnated $PrBaCo_2O_{5+\delta}$ composite cathode for proton conducting SOFCs", *Ceram. Int.*, **40** [8] (2014) 13753–13756.
19. J. Choi, B. Kim, D. Shin, "Performance evaluation of $Sm_{0.5}Sr_{0.5}CoO_{3-\delta}$ fibers with embedded $Sm_{0.2}Ce_{0.8}O_{1.9}$ particles as a solid oxide fuel cell composite cathode", *J. Eur. Ceram. Soc.*, **33** [12] (2013) 2269–2273.
20. I. Ismail, N. Osman, A.M.M. Jani, "$La_{0.6}Sr_{0.4}Co_{0.2}Fe_{0.8}O_{3-\delta}$ powder: A simple microstructure modification strategy for enhanced cathode electrochemical performance", *J. Sol-Gel Sci. Technol.*, **94** (2020) 435–447.
21. N.A. Abdullah, S. Hasan, N. Osman, "Role of CA-EDTA on the synthesizing process of cerate-zirconate ceramics electrolyte", *J. Chemistry*, **2013** (2013) 1–7.
22. N. Osman, N.A. Mazian, S. Affandi, N.W. Mazain, "Optimization of electrolyte performance by tailoring the structure and morphology of $Ba(Ce,Zr)O_3$ ceramics with different types of surfactants", *Ceram. Int.*, **46** [17] (2020) 27401–27409.
23. Y. Xia, Z. Jin, H. Wang, Z. Gong, H. Lv, R. Peng, W. Liu, L. Bi, "A novel cobalt-free cathode with triple-conduction for proton-conducting solid oxide fuel cells with unprecedented performance", *J. Mater. Chem. A*, **7** [27] (2019) 16136–16148.
24. N. Osman, I. Ismail, A.A. Samat, A.M.M. Jani, "Reactivity study of $LaSrCoFeO_3$-$Ba(Ce,Zr)O_3$ composite cathode material", *Mater. Sci. Forum*, **846** (2016) 58–62.
25. V.R. Ouhadi, R.N. Yong, "Impact of clay microstructure and mass absorption coefficient on the quantitative mineral identification by XRD analysis", *Appl. Clay Sci.*, **23** [1] (2003) 141–148.
26. S.B. Adler, J. Lane, B. Steele, "Electrode kinetics of porous mixed-conducting oxygen electrodes", *J. Electrochem. Soc.*, **143** [11] (1996) 3554–3564.

27. T. Wu, R. Peng, C. Xia, "$Sm_{0.5}Sr_{0.5}CoO_{3-\delta}$-$BaCe_{0.8}Sm_{0.2}O_{3-\delta}$ composite cathodes for proton-conducting solid oxide fuel cells", *Solid State Ionics*, **179** [27] (2008) 1505–1508.
28. J.H. Kim, M. Cassidy, J.T.S. Irvine, J. Bae, "Electrochemical investigation of composite cathodes with $SmBa_{0.5}Sr_{0.5}Co_2O_{5+\delta}$ cathodes for intermediate temperature-operating solid oxide fuel cell", *Chem. Mater*., **22** [3] (2009) 883–892.
29. S. Ricote, N. Bonanos, P.M. Rørvik, C. Haavik, "Microstructure and performance of $La_{0.58}Sr_{0.4}Co_{0.2}Fe_{0.8}O_{3-\delta}$ cathodes deposited on $BaCe_{0.2}Zr_{0.7}Y_{0.1}O_{3-\delta}$ by infiltration and spray pyrolysis", *J. Power Sources*, **209** (2012) 172–179.
30. C. Yang, X. Zhang, H. Zhao, Y. Shen, Z. Du, C. Zhang, "Electrochemical properties of $BaZr_{0.1}Ce_{0.7}Y_{0.1}Yb_{0.1}O_{3-\delta}$-$Nd_{1.95}NiO_{4+\delta}$ composite cathode for protonic ceramic fuel cells", *Int. J. Hydrogen Energy*, **40** [6] (2015) 2800–2807.
31. J. Dailly, F. Mauvy, M. Marrony, M. Pouchard, "Electrochemical properties of perovskite and A_2MO_4-type oxides used as cathodes in protonic ceramic half cells", *J. Solid State Electrochem*., **15** [2] (2011) 245–251.
32. S.-W. Baek, J. Bae, Y.-S. Yoo, "Cathode reaction mechanism of porous-structured $Sm_{0.5}Sr_{0.5}CoO_{3-\delta}$ and $Sm_{0.5}Sr_{0.5}CoO_{3-\delta}/Sm_{0.2}Ce_{0.8}O_{1.9}$ for solid oxide fuel cells", *J. Power Sources*, **193** [2] (2009) 431–440.
33. M. Zhang, M. Yang, Z. Hou, Y. Dong, M. Cheng, "A bi-layered composite cathode of $La_{0.8}Sr_{0.2}MnO_3$-YSZ and $La_{0.8}Sr_{0.2}MnO_3$-$La_{0.4}Ce_{0.6}O_{1.8}$ for IT-SOFCs", *Electrochim. Acta*, **53** [15] (2008) 4998–5006.
34. T. Wu, W. Liu, X. Liu, G. Meng, "Cathode processes and materials for solid oxide fuel cells with proton conductors as electrolytes", *J. Mater. Chem*., **20** [30] (2010) 6218–6225.
35. D. Chen, L. LU, J. Li, Z. Yu, W. Kong, H. Zhu, "Percolation micro-model to predict the effective properties of the composite electrode with poly-dispersed particle sizes", *J. Power Sources*, **196** [6] (2011) 3178–3185.
36. C.-Y. Yoo, D.S. Yun, S.-Y. Park, J. Park, J.H. Joo, H. Park, M. Kwak, J.H. Yu, "Investigation of electrochemical properties of model lanthanum strontium cobalt ferrite-based cathodes for proton ceramic fuel cells", *Electrocatalysis*, **7** [4] (2016) 280–286.
37. G. Li, Y. Zhang, Y. Ling, B. He, J. Xu, L. Zhao, "Probing novel triple phase conducting composite cathode for high performance protonic ceramic fuel cells", *Int. J. Hydrogen Energy*, **41** [9] (2016) 5074–5083.
38. M. Li, M. Ni, F. Su, C. Xia., "Proton conducting intermediate-temperature solid oxide fuel cells using new perovskite type cathodes", *J. Power Sources*, **260** (2014) 197–204.
39. R.R. Liu, S.H. Kim, S.Taniguchi, T. Oshima, Y. Shiratori, K. Ito, K. Sasaki, "Influence of water vapor on long-term performance and accelerated degradation of solid oxide fuel cell cathodes", *J. Power Sources*, **196** [17] (2011) 7090–7096.
40. H. Taherparvar, J.A. Kilner, R.T. Baker, M. Sahibzada, "Effect of humidification at anode and cathode in proton-conducting SOFCs", *Solid State Ionics*, **162-163** (2003) 297–303.
41. M. Kim, H. Muroyama, T. Matsui, K. Eguchi, "Influence of water vapor on performance degradation and microstructural change of $(La,Sr)(Co,Fe)O_{3-\delta}$ cathode", *J. Electrochem. Soc*., **166** [16] (2019) F1269.
42. L. dos Santos-Gómez, J.M. Porras-Vazquez, E.R. Losilla, F. Martin, J.R. Ramos-Barrado, D. Marrero-Lopez, "Stability and performance of $La_{0.6}Sr_{0.4}Co_{0.2}Fe_{0.8}O_{3-\delta}$ nanostructured cathodes with $Ce_{0.8}Gd_{0.2}O_{1.9}$ surface coating", *J. Power Sources*, **347** (2017) 178–185.
43. F. Deganello, V. Esposito, M. Miyayama, E. Traversa, "Cathode performance of nanostructured $La_{1-a}Sr_aCo_{1-b}Fe_bO_{3-x}$ on a $Ce_{0.8}Sm_{0.2}O_2$ electrolyte prepared by citrate-nitrate autocombustion", *J. Electrochem. Soc*., **154** [2] (2007) A89–A96.
44. G. Li, B. He, Y. Ling, J. Xu, L. Zhao, "Highly active YSB infiltrated LSCF cathode for proton conducting solid oxide fuel cells", *Int. J. Hydrogen Energy*, **40** [39] (2015) 13576–13582.
45. M.S. Wang, J.X. Wang, C.R. He, Y.J. Xue, H.M. Miao, Q. Wang, W.G. Wang, "A novel composite cathode $La_{0.6}Sr_{0.4}CoO_{3-\delta}$-$BaZr_{0.1}Ce_{0.7}Y_{0.1}Yb_{0.1}O_{3-\delta}$ for intermediate temperature solid oxide fuel cells", *Ceram. Int*., **41** [3, Part B] (2015) 5017–5025.
46. V. Vert, C. Solís, J. Serra, "Electrochemical properties of PSFC-BCYb composites as cathodes for proton conducting solid oxide fuel cells", *Fuel Cells*, **11** [1] (2011) 81–90.
47. B. Lin, H. Ding, Y. Dong, S. Wang, X. Zhang, D. Fang, G. Meng, "Intermediate-to-low temperature protonic ceramic membrane fuel cells with $Ba_{0.5}Sr_{0.5}Co_{0.8}Fe_{0.2}O_{3-\delta}$-$BaZr_{0.1}Ce_{0.7}Y_{0.2}O_{3-\delta}$ composite cathode", *J. Power Sources*, **186** [1] (2009) 58–61.
48. X. Lu, Y. Chen, Y. Ding, B. Lin, "A cobalt-free $Sm_{0.5}Sr_{0.5}FeO_{3-\delta}$-$BaZr_{0.1}Ce_{0.7}Y_{0.2}O_{3-\delta}$ composite cathode for proton-conducting solid oxide fuel cells", *Int. J. Hydrogen Energy*, **37** [10] (2012) 8630–8634.
49. E. Fabbri, S. Licoccia, E. Traversa, E.D. Wachsman, "Composite cathodes for proton conducting electrolytes", *Fuel Cells*, **9** [2] (2009) 128–138.